Understanding the electrochemical behaviour of LSM-based SOFC cathodes. Part II - Mechanistic modelling and physically-based interpretation

UNDERSTANDING THE ELECTROCHEMICAL BEHAVIOUR OF LSM-BASED SOFC CATHODES.

PART II - MECHANISTIC MODELLING AND PHYSICALLY-BASED INTERPRETATION

A. Bertei[a*], M. P. Carpanese[b], D. Clematis[b], A. Barbucci[b], M. Z. Bazant[c,d], C. Nicolella[a]

[a]Department of Civil and Industrial Engineering, University of Pisa, Largo Lucio Lazzarino 2, 56126 Pisa, Italy

[b]Department of Civil, Chemical and Environmental Engineering, University of Genova, P.le J.F. Kennedy 1, 16129 Genova, Italy

[c]Department of Chemical Engineering, Massachusetts Institute of Technology, Ames Street 25, MA 02139 Cambridge, MA, USA

[d]Department of Mathematics, Massachusetts Institute of Technology, Memorial Drive 182, MA 02139 Cambridge, MA, USA

Version accepted by:

SOLID STATE IONICS

(SEPTEMBER 2016)[⊥]

[*] Corresponding author: telephone +39-050 221 7814; fax +39-050 221 7866; e-mail antonio.bertei@for.unipi.it

[⊥] *Abbreviations*: LSM = strontium-doped lanthanum manganite; ORR = oxygen reduction reaction; TPB = three-phase boundary; YSZ = yttria-stabilized zirconia.

Abstract

This study presents a physically-based model for the impedance simulation of the oxygen reduction reaction in porous strontium-doped lanthanum manganite (LSM) cathodes. The model describes the surface mechanism only, taking into account the co-limited adsorption/diffusion of oxygen and the charge-transfer reaction at the three-phase boundary (TPB). After calibration with experimental impedance spectra, the model is used to identify the transition of kinetic regime from the surface to the bulk path mechanism, which occurs at cathodic dc bias of ca. 0.2V within 700-800°C. The transition is highlighted by a significant decrease in impedance and the appearance of a low-frequency inductive loop. The model consistently reproduces the impedance spectra before the transition of kinetic regime with a single set of parameters, allowing for the deconvolution of two features, one associated to the co-limited adsorption/diffusion process (ca. 5Hz) and another minor contribution due to the charge-transfer at the TPB (ca. 35Hz). The model and its parameters, which quantitatively agree with the literature, can be used as a basis to optimize the microstructural and surface properties of technical LSM-based cathodes, showing that the TPB length is not the main parameter to be maximized.

Keywords: LSM; oxygen reduction reaction; surface path; modeling; impedance spectroscopy.

1. Introduction

Solid oxide fuel cells (SOFCs) are a promising technology to produce electric power from the electrochemical conversion of a fuel. Besides low emission of pollutants, fuel flexibility and capability to be scaled up from kW to MW-range applications, SOFCs can operate in principle with high efficiency of energy conversion [1–3]. However,

especially for intermediate and low temperature operation, the electrochemical performance is still far from the theoretical upper bound of efficiency. One of the causes of the non-optimal performance stems from the polarization resistance of the electrodes. In particular, in hydrogen-fuelled SOFCs, the activation of the oxygen reduction reaction (ORR) in the cathode represents the main source of energy loss [4,5]. Despite extensive research in this field, the fundamentals of the ORR remain still unclear [4,6]. A thorough understanding of the kinetic mechanism would allow researchers to optimize the catalytic and microstructural properties of electrode materials in order to reduce the activation resistance and thus improve the performance of the whole cell [7].

For one of the most studied and commonly used cathode materials such as strontium-doped lanthanum manganite (LSM), there are several experimental indications suggesting two kinetic regimes for the ORR: a surface path and a bulk path. In the surface path, molecular oxygen is adsorbed onto the LSM and diffuses on the surface towards the three-phase boundary (TPB), wherein it is incorporated into the electrolyte, which is typically yttria-stabilized zirconia (YSZ). On the other hand, in the bulk path oxygen is reduced at the LSM surface, then ions diffuse within the LSM grains or along grain boundaries and reach the electrode/electrolyte interface. The transition between the two regimes depends on the operating temperature and the applied bias: the surface path is favoured at low temperature (below ca. 700°C) and low cathodic overpotential (below ca. 0.2V), while the bulk path at high temperature and high cathodic overpotential [4,8–11].

Recently modelling studies [12–18] have emerged to provide a mechanistic interpretation and quantitatively corroborate these experimental evidences, providing deeper insights than those obtained from the application of phenomenological equivalent circuits [19–21]. Nielsen and Hjelm [15] applied the porous electrode

theory to interpret the impedance spectra of composite LSM/YSZ cathodes over a wide range of temperatures. Based on their analysis, the authors rejected the adsorption and surface diffusion mechanism proposed in the literature. However, it must be mentioned that they used a non-physical element, such as the constant phase element (CPE), to describe the ORR in their de Levie model, thus they did not completely elucidate the reaction mechanism. Liu and co-workers [12–14] published a series of papers presenting a physically-based numerical model taking into account both the surface and bulk path mechanisms. The model was applied to simulate both polarization curves and impedance spectra, focussing on the transition overpotential between surface and bulk path, identified between 0.2 and 0.4V under cathodic bias. Despite the valuable insights provided by these papers, further efforts are necessary to estimate the parameters required by the model. A valid study regarding the parameter estimation was made by Fu et al. [16], who proposed an impedance model of the surface path. Their model showed to consistently fit the impedance spectra in LSM/YSZ electrodes for different microstructural characteristics and oxygen partial pressures, although their results are limited to open circuit conditions. More recently, Banerjee and Deutschmann [22,23] have considered two elementary kinetic models of the ORR, discussing about their validity and sensitivity for composite LSM/YSZ cathodes.

Despite the good achievements reached so far, a detailed mechanistic study on the transition of kinetic regime with overpotential, supported by experimental data in real LSM cathodes, is missing. In this study, a combined experimental and modelling study based on impedance spectroscopy (EIS) analysis is presented in order to quantitatively confirm the transition from surface to bulk path. The second part of this series of papers focuses on model development, mechanistic interpretation and identification of the transition overpotential. The model, which is an extension of that proposed by Fu

et al. [16] and is similar to that developed by Kenney and Karan [17], which in turn is based upon van Heuveln et al. [24,25], considers the surface path only and it is kept as simple as possible to reduce the number of unknown parameters.

The paper is organized as follows. In Section 2 the model for the simulation of impedance spectra is described. The results of the study, concerning model validation, discussion of parameters, mechanistic interpretation of experimental data and identification of the transition of kinetic regime, are presented in Section 3. The general conclusions of the study are reported in Section 4.

2. Modelling

The model represents an extension of that proposed by Fu et al. [16] and simulates only the surface path. The ORR mechanism is decoupled into two steps: co-limited adsorption/diffusion of oxygen onto the electron-conducting phase and charge-transfer reaction at the TPB with the electrolyte.

Figure 1 provides a schematic illustration of the phenomena considered by the model for a porous LSM electrode on YSZ electrolyte. Molecular oxygen is adsorbed onto the surface of the LSM (i.e., the electron-conducting phase *el*) following a dissociative adsorption mechanism:

$$O_{2(g)} \leftrightarrow 2O_{(el,s)} \tag{1}$$

Oxygen adatoms diffuse on the surface of the cathode and reach the TPB at the electrolyte interface, wherein they undergo a charge transfer reaction with the electrons carried by the electronic conductor, as follows [17]:

$$O_{(el,s)} + 2e^{-}_{(el)} \leftrightarrow O^{2-}_{(io)} \quad (2)$$

to form oxygen ions, which are incorporated into the electrolyte (i.e., the ionic conductor *io*, which is YSZ in this case).

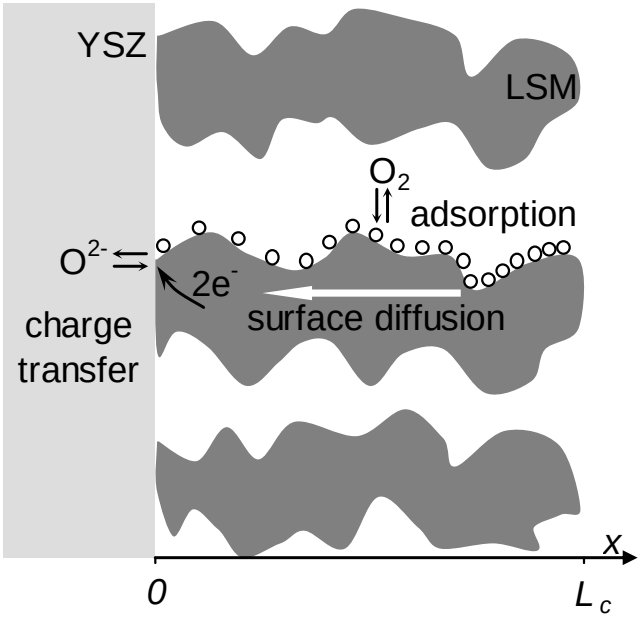

Figure 1. Schematic representation of the surface path of the ORR considered by the model, showing the co-limited adsorption/diffusion of oxygen on LSM followed by the charge-transfer at the TPB at the electrolyte interface.

These processes are mathematically described by the model, which is presented in Sections 2.1 and 2.2 in time and frequency domain, respectively. Before entering into the details, it is worth summarizing the main assumptions of the model:

- the adsorption/desorption reaction follows a dissociative Langmuir kinetics [17];
- the Fick law is adopted to describe the surface diffusion of oxygen adatoms [26];

- the charge-transfer reaction takes place at the TPB only and follows a linear Butler-Volmer kinetics [27]. The elementary steps of the reaction are not explicitly simulated in order to reduce the complexity of the model. Nevertheless, the formation of reaction intermediates in the charge-transfer reaction at the TPB is taken into account with a linear capacitance;
- electron and gas transport along the electrode thickness are neglected as they are expected to be much faster than the adsorption/diffusion process in the porous LSM electrodes considered in this study;
- the electrode microstructure is not explicitly resolved, instead it is treated as a continuum of LSM and porous phase. Material-specific and microstructural properties are assumed to be uniform, resulting in a 1D model along the cathode thickness;
- uniform temperature is considered in the model.

2.1 Model equations in time domain

This Section describes the model equations for EIS simulation of a porous LSM electrode in time domain. In the model, the coordinate x represents the distance from the electrolyte interface: the electrode/electrolyte interface is located at $x = 0$, while $x = L_c$ represents the cathode thickness (see Figure 1). The list of symbols used during the model derivation is reported at the end of paper.

The Faradaic contribution of the charge-transfer reaction is assumed to occur at the TPB at $x = 0$, according to the Butler-Volmer kinetics [27]:

$$i_{TPB} = i_{00}\left(\frac{\theta_0}{1-\theta_0}\right)^{1-\alpha}\left\{\exp\left[\alpha\frac{2F}{RT}\eta_{act}\right]-\exp\left[-(1-\alpha)\frac{2F}{RT}\eta_{act}\right]\right\} \quad (3a)$$

$$\eta_{act} = -\frac{RT}{2F}\ln\left(\frac{\theta_{eq}}{\theta_0}\frac{1-\theta_0}{1-\theta_{eq}}\right) - \left(V_{el} - V_{io}\right) \tag{3b}$$

In Eq. (3), a unitary activity of oxygen ions in the electrolyte is assumed [28]. On the other hand, the LSM surface is treated as an ideal solution of free sites and oxygen adatoms, whose activity is thus equal to $a_\theta = \theta/(1-\theta)$ according to non-equilibrium thermodynamics [26]. θ_0 represents the surface coverage fraction of oxygen adatoms at $x = 0$ while θ_{eq} is the surface coverage fraction in equilibrium with the gas phase, that is, in open circuit condition (see Eq. (7)). The activation overpotential η_{act}, considered positive for cathodic current production, takes into account the equilibrium potential difference [29], which is basically a concentration contribution [30,31].

Since the electron transport is neglected, the difference $-(V_{el}-V_{io})$, calculated at $x = 0$, represents the total overpotential applied to the cathode η_{cat}. In EIS simulations, η_{cat} consists of a steady-state dc overpotential η_{bias} and a sinusoidal ac perturbation $\Delta\eta_{ac}\cdot e^{j\omega t}$. In addition, as the activation overpotential is expected to be small, the Butler-Volmer kinetics can be linearized to simplify the expression. Thus, Eq. (3) becomes:

$$i_{TPB} = i_{00}\left(\frac{\theta_0}{1-\theta_0}\right)^{1-\alpha}\frac{2F}{RT}\eta_{act} \tag{4a}$$

$$\eta_{act} = -\frac{RT}{2F}\ln\left(\frac{\theta_{eq}}{\theta_0}\frac{1-\theta_0}{1-\theta_{eq}}\right) + \eta_{cat} \quad \text{with} \quad \eta_{cat} = \eta_{bias} + \Delta\eta_{ac}\cdot e^{j\omega t} \tag{4b}$$

Within the electrode thickness, oxygen adsorbs onto the LSM surface and then diffuses towards the electrolyte to take part to the charge-transfer reaction at the TPB (see Figure 1). According to Langmuir dissociative adsorption and Fick surface

diffusion, the conservation of adsorbed oxygen atoms along the electrode thickness results as follows:

$$\Gamma a_{el}^{v} \frac{\partial \theta}{\partial t} = -\frac{\partial N_O^{surf}}{\partial x} + \Gamma a_{el}^{v} k_{des}\left(Kp_{O2}(1-\theta)^2 - \theta^2\right) \tag{5a}$$

$$N_O^{surf} = -\Gamma a_{el}^{v} D_s^{eff} \frac{\partial \theta}{\partial x} \tag{5b}$$

where Eq. (5b) represents the flux of oxygen adatoms per unit of electrode area. In Eq. (5) Γ is the number of adsorption sites per unit of LSM surface area while a_{el}^{v} is the LSM surface area exposed to gas phase per unit of electrode volume. The effective diffusivity D_s^{eff} in Eq. (5b) takes into account the surface diffusivity of oxygen adatoms corrected for the surface tortuosity factor $D_s^{eff} = D_s / \tau_s$ [32].

Eq. (5) is coupled with the following boundary conditions that, along with Eq. (4), close the mathematical problem:

$$x = 0 \rightarrow N_O^{surf} = -\frac{i_{TPB}\lambda_{TPB}^{s}}{2F} - \frac{c_{TPB}\lambda_{TPB}^{s}}{2F}\frac{\partial \eta_{act}}{\partial t} \tag{6a}$$

$$x = L_c \rightarrow N_O^{surf} = 0 \tag{6b}$$

Eq. (6a) states that the flux that reaches the TPB is converted into two contributions: a Faradaic contribution, which is related to the charge-transfer reaction Eq. (4), and a capacitive contribution, which takes into account the formation of reaction intermediates at the TPB, proportional to the time derivative of the activation overpotential. c_{TPB} in Eq. (6a) is a lumped parameter to take into account the buffer effect of reaction intermediates associated to the charge-transfer reaction at TPB,

which is expected to occur in a multi-step process. Both the Faradaic and capacitive contributions are assumed to be proportional to λ_{TPB}^{s}, which is the TPB length per unit of interfacial area between electrode and electrolyte.

Finally, the equilibrium surface coverage θ_{eq} at open-circuit equilibrium in Eq. (4b) is calculated according to the Langmuir equilibrium [16]:

$$\theta_{eq} = \frac{\sqrt{Kp_{O2}}}{1+\sqrt{Kp_{O2}}} \tag{7}$$

The current circulating in the cathode at the electrode/electrolyte interface is equal to the electrochemical contribution due to Eq. (6a) plus the current associated to the electric double-layer capacitance between LSM and YSZ as follows:

$$I = -N_O^{surf}\Big|_{x=0} 2F + c_{dl} a_{dl}^{s} \frac{\partial\left(V_{io} - V_{el}\right)}{\partial t} \tag{8}$$

The system of Eqs. (4-6) can be solved at steady-state by neglecting all the time-dependent terms in order to obtain the electrode response to the dc overpotential η_{bias}. The steady-state solution, represented with a bar sign $\bar{}$, satisfies the following equations:

$$0 = -\frac{d\bar{N}_O^{surf}}{dx} + \Gamma a_{el}^{v} k_{des}\left(Kp_{O2}\left(1-\bar{\theta}\right)^2 - \bar{\theta}^2\right) \tag{9a}$$

$$\bar{N}_O^{surf} = -\Gamma a_{el}^{v} D_s^{eff} \frac{d\bar{\theta}}{dx} \tag{9b}$$

$$x = 0: \quad \bar{i}_{TPB} = \underbrace{i_{00}\left(\frac{\bar{\theta}_0}{1-\bar{\theta}_0}\right)^{1-\alpha}\frac{2F}{RT}}_{1/r_{TPB}}\bar{\eta}_{act} = \frac{\bar{\eta}_{act}}{r_{TPB}} \tag{10a}$$

$$\bar{\eta}_{act} = -\frac{RT}{2F}\ln\left(\frac{\theta_{eq}}{\bar{\theta}_0}\frac{1-\bar{\theta}_0}{1-\theta_{eq}}\right) + \eta_{bias} \tag{10b}$$

$$\bar{N}_O^{surf} = -\frac{\bar{i}_{TPB}\lambda_{TPB}^s}{2F} \tag{10c}$$

$$x = L_c: \quad \bar{N}_O^{surf} = 0 \tag{11}$$

and allows for the calculation of the dc current density circulating in the cathode upon the application of the bias η_{bias}, as follows:

$$\bar{I} = -\bar{N}_O^{surf}\Big|_{x=0} 2F = \bar{i}_{TPB}\lambda_{TPB}^s \tag{12}$$

The steady-state solution provides some interesting insights. For example, Eq. (10b) can be rearranged as follows:

$$\eta_{bias} = \bar{\eta}_{act} + \frac{RT}{2F}\ln\left(\frac{\theta_{eq}}{\bar{\theta}_0}\frac{1-\bar{\theta}_0}{1-\theta_{eq}}\right) \tag{13}$$

In this form, Eq. (13) shows that the applied dc overpotential η_{bias} is split into two contributions [30]: an electrochemical contribution, equal to the activation overpotential $\bar{\eta}_{act}$, which activates the charge-transfer reaction, and a concentration contribution, equal to the equilibrium potential difference, which is indicative of the potential loss associated to the adsorption/diffusion process. The relative proportion

between these two contributions indicates if the total energy loss in the ORR is mainly due to the charge-transfer reaction or to the adsorption/diffusion process.

In Eq. (10a), the term in curly bracket represents the inverse of the charge-transfer resistance referred per unit of TPB length r_{TPB}. Notably, r_{TPB} depends on $\bar{\theta}_0$ for $\alpha \neq 1$, which in turns depends on the applied dc bias. In particular, for $\alpha < 1$ r_{TPB} increases as $\bar{\theta}_0$ decreases. $\bar{\theta}_0$ decreases as the applied dc bias increases since oxygen adatoms are removed from LSM surface by the charge-transfer reaction, thus r_{TPB} increases as η_{bias} increases and becomes infinite when $\bar{\theta}_0$ approaches 0, which corresponds to the limiting current density that can be drawn by the adsorption/diffusion surface path. This point is further discussed in Section 3.3, especially in Figure 9.

2.2 Model equations in frequency domain

The mathematical system represented by Eqs. (4-6) is converted in this Section in frequency domain in order to compute the impedance of the electrode.

Consider a small sinusoidal perturbation $\Delta\eta_{ac}$ to the cathode overpotential (see Eq. (4b)), applied as a boundary condition. Such a perturbation produces small perturbations of $\Delta\theta$, $\Delta\eta_{act}$, Δi_{TPB}, ΔN_O^{surf} and, ultimately, a current perturbation ΔI. For the generic variable ζ the perturbation $\Delta\zeta$ is defined as the local deviation from the steady-state solution as follows [33,34]:

$$\zeta - \bar{\zeta} = \delta\zeta \cdot e^{j(\omega t+\varphi)} = \Delta\zeta \cdot e^{j\omega t} \quad \text{with } \delta\zeta << \bar{\zeta} \tag{14}$$

By applying Eq. (14) into the system of Eqs. (4-6), after linear Taylor expansion and upon subtraction of the steady-state solution [35], the system of equations in frequency domains results as follows:

$$j\omega\Gamma a_{el}^{v}\Delta\theta = -\frac{d\Delta N_O^{surf}}{dx} - 2k_{des}\Gamma a_{el}^{v}\left(Kp_{O2} + \bar{\theta}(1-Kp_{O2})\right)\Delta\theta \quad (15a)$$

$$\Delta N_O^{surf} = -\Gamma a_{el}^{v} D_s^{eff}\frac{d\Delta\theta}{dx} \quad (15b)$$

$$x = 0:\ \Delta i_{TPB} = i_{00}\left(\frac{\bar{\theta}_0}{1-\bar{\theta}_0}\right)^{1-\alpha}\frac{2F}{RT}\Delta\eta_{act} + i_{00}\frac{(1-\alpha)}{\left(\frac{\bar{\theta}_0}{1-\bar{\theta}_0}\right)^{\alpha}\left(1-\bar{\theta}_0\right)^2}\frac{2F}{RT}\bar{\eta}_{act}\Delta\theta_0 \quad (16a)$$

$$\Delta\eta_{act} = \frac{RT}{2F}\frac{1}{\bar{\theta}_0\left(1-\bar{\theta}_0\right)}\Delta\theta_0 + \Delta\eta_{ac} \quad (16b)$$

$$\Delta N_O^{surf} = -\frac{\Delta i_{TPB}\lambda_{TPB}^{s}}{2F} - j\omega\frac{c_{TPB}\lambda_{TPB}^{s}}{2F}\Delta\eta_{act} \quad (16c)$$

$$x = L_c:\ \Delta N_O^{surf} = 0 \quad (17)$$

where the terms of order equal or higher than $\Delta\zeta^2$ have been neglected.

The current perturbation can be calculated from the conversion of Eq. (8) in frequency domain as follows:

$$\Delta I = -\Delta N_O^{surf}\Big|_{x=0} 2F + j\omega c_{dl}a_{dl}^{s}\Delta\eta_{ac} \quad (18)$$

The impedance of the cathode is calculated by dividing the ac voltage perturbation by the current perturbation:

$$Z(\omega) = Z_{\mathrm{Re}}(\omega) + jZ_{\mathrm{Im}}(\omega) = \frac{\Delta\eta_{ac}}{\Delta I} \quad (19)$$

which can be calculated for different frequencies f, where $f = \omega/(2\pi)$. Finally, the ohmic resistance of the electrolyte is added in series to directly compare model results with experimental data.

The system in frequency domain Eqs. (15-19) depends on the steady-state solution $\bar{\theta}$ (see Eqs. (15a), (16a) and (16b)), or, in other words, the impedance Z depends on the applied dc bias η_{bias}. For each applied dc bias η_{bias}, first the steady-state solution is computed by solving Eqs. (9-11), then Eqs. (15-19) are solved for each frequency to compute the impedance of the cathode. The commercial finite-element software COMSOL Multiphysics [36] is used in this study to perform the numerical simulations.

The impedance of the electrode can be schematized by the equivalent circuit represented in Figure 2. It is noteworthy that the equivalent circuit provides only a pictorial representation of the different contributions of electrode impedance and it is not used to compute the impedance. Indeed, the value of the elements in the circuit must be calculated numerically, as both $Z_{ads/diff}$ and R_{TPB} depend on frequency and applied dc bias in a complex way which cannot be represented analytically.

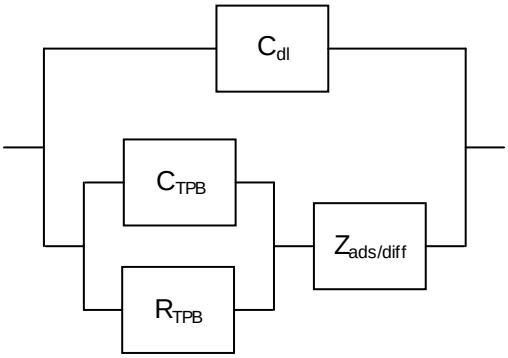

Figure 2. Schematic representation of model equations representing the impedance contributions of surface path of the ORR mechanism. Note that this circuit is not used to compute the impedance, which is obtained by solving numerically the system of Eqs. (5-11) and (15-19).

3. Results and discussion

3.1 Microstructural parameters

The model presented in Section 2 contains parameters such as λ_{TPB}^{s}, a_{dl}^{s}, a_{el}^{v}, τ_s and L_c which are related to the microstructure of the cathode. These parameters are obtained by numerically reconstructing the electrode microstructure with a validated packing algorithm, with input parameters obtained from SEM images. For a comprehensive description of microstructural model the reader is referred to Refs. [37–39] and to Part 1 for SEM images.

The list of microstructural parameters used in the model and in the reconstruction is reported in Table 1. The thickness, porosity and mean particle size of LSM particles are obtained from the image analysis of polished cross-sections and top views of the electrode. This information represents the input parameters of the microstructural model, which estimates the TPB length and interfacial area, as well as the surface area of LSM per unit volume. The surface tortuosity factor τ_s is estimated according to Zalc et al. [32].

The microstructural parameters refer to the cathode sintered at 1150°C analysed in Part 1, whose impedance is discussed in the following Sections.

Table 1. Microstructural and geometrical properties of the LSM porous electrode sintered at 1150°C.

Parameter	**Value**	**Reference**
Thickness, L_c	2.7μm	Image analysis, Part 1
Porosity, ϕ	0.337	Image analysis, Part 1
Mean particle size, d_{part}	2μm	Image analysis, Part 1
TPB per unit area, λ_{TPB}^{s}	0.849μm^{-1}	Numerical reconstruction, this study
Interfacial area per unit area, a_{dl}^{s}	0.669	Numerical reconstruction, this study
Surface area per unit volume, a_{el}^{v}	1.106μm^{-1}	Numerical reconstruction, this study
Surface tortuosity factor, τ_s	2.496	Zalc et al. [32]

3.2 Calibration of the model

The model is calibrated at OCV by comparing model simulations with experimental EIS data measured at different temperatures and oxygen partial pressures. The calibration allows for the fitting of the unknown material-specific parameters of the ORR, which are k_{des}, K, D_s, i_{00}, c_{TPB}, α and Γ (see Table 2). Except for α and Γ, which are assumed to be constant in all the experimental conditions, the other parameters are expected to depend on temperature while being independent of oxygen partial pressure. In this study, the unknown parameters are fitted according to a global calibration approach. This means that model parameters are not tuned to fit each single impedance spectrum, instead a global fitting of all the spectra is searched by allowing k_{des}, K, D_s, i_{00} and c_{TPB} to vary with temperature while being constant with different p_{O2}. While this global calibration approach does not allow the model to perfectly reproduce the experimental data in each impedance spectrum, it guarantees the self-consistency of the fitting throughout all the data set. A complex non-linear least square fitting is used to minimize the sum of squared residuals, weighted for the reciprocal of the experimental magnitude of impedance [40].

The calibration of the model for different temperatures at OCV and p_{O2} = 0.21atm is reported in Figure 3. The polarization resistance of the electrode, which is comparable to that reported in similar studies [25,41], is high because the cathode is not optimized for performance, such as a composite LSM/YSZ electrode would be. Employing a porous LSM cathode with a relatively simple microstructure simplifies the model calibration because the impedance contribution of the ORR kinetics is amplified in the EIS data. This experimental setup allows the model to focus on the ORR kinetics only, thus avoiding any ambiguity in the deconvolution of the additional charge and mass

transport phenomena that would be present in a composite LSM/YSZ cathode for technically relevant applications.

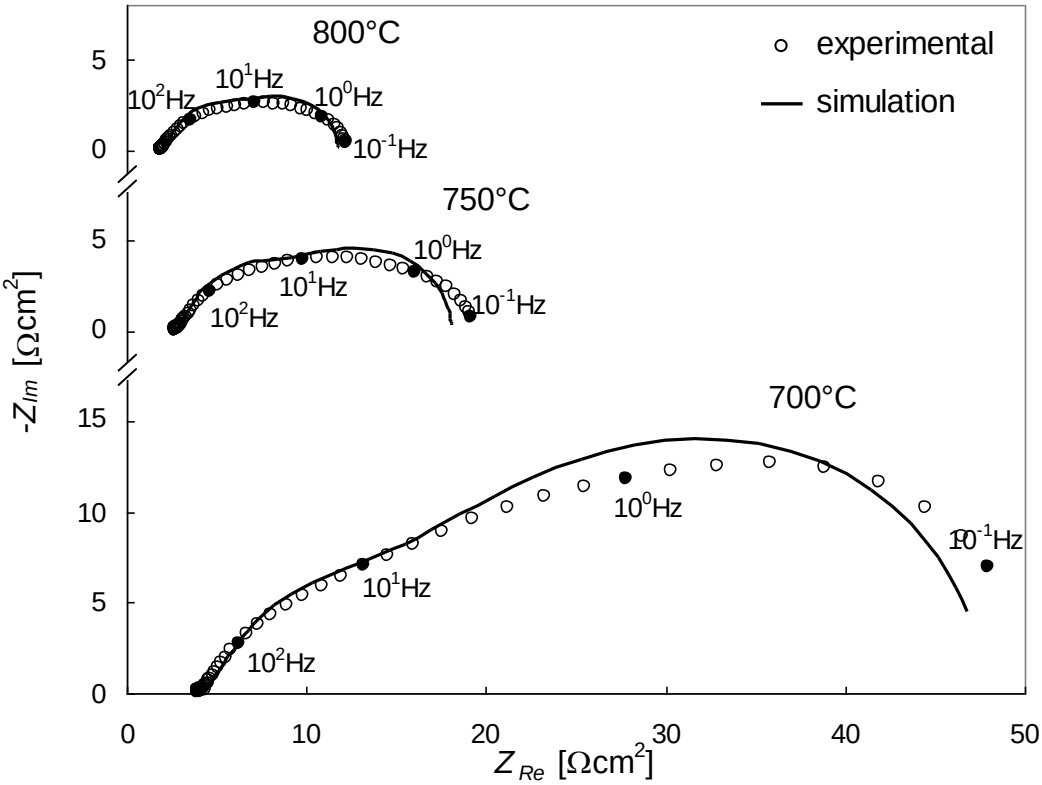

Figure 3. Calibration of the model (lines) with experimental data (circles) for different temperatures at OCV and p_{O2} = 0.21atm.

In the whole range of temperatures (700-800°C), the experimental impedance shows a depressed shape. Especially at 700°C, the impedance resembles the sum of two different contributions: a smaller contribution at medium frequency and a bigger one at low frequency. The presence of two impedance contributions is supported by model simulations in the next Section (see Figure 10). As the temperature increases, both the contributions shrink, thus the total polarization resistance decreases as also reported in the literature [4,8,42]. The contribution of the low-frequency feature shrinks faster than that at medium frequency, and at 800°C the two contributions have a rather similar magnitude, resulting in a single depressed shape. The characteristic frequency of the

cathode falls between 0.5 and 10Hz, which is consistent with the literature [4,16,17,41,43,44], and increases as temperature increases, meaning that the physical-chemical processes that build up the impedance become faster as temperature increases.

The impedance spectra for different oxygen partial pressures are reported in Figure 4 at OCV and 750°C. As the oxygen partial pressure decreases, the polarization resistance increases, as often reported in the literature [4,16,43]. In particular, while the impedance is almost unaffected in the high frequency range, the low-frequency feature increases as p_{O2} decreases.

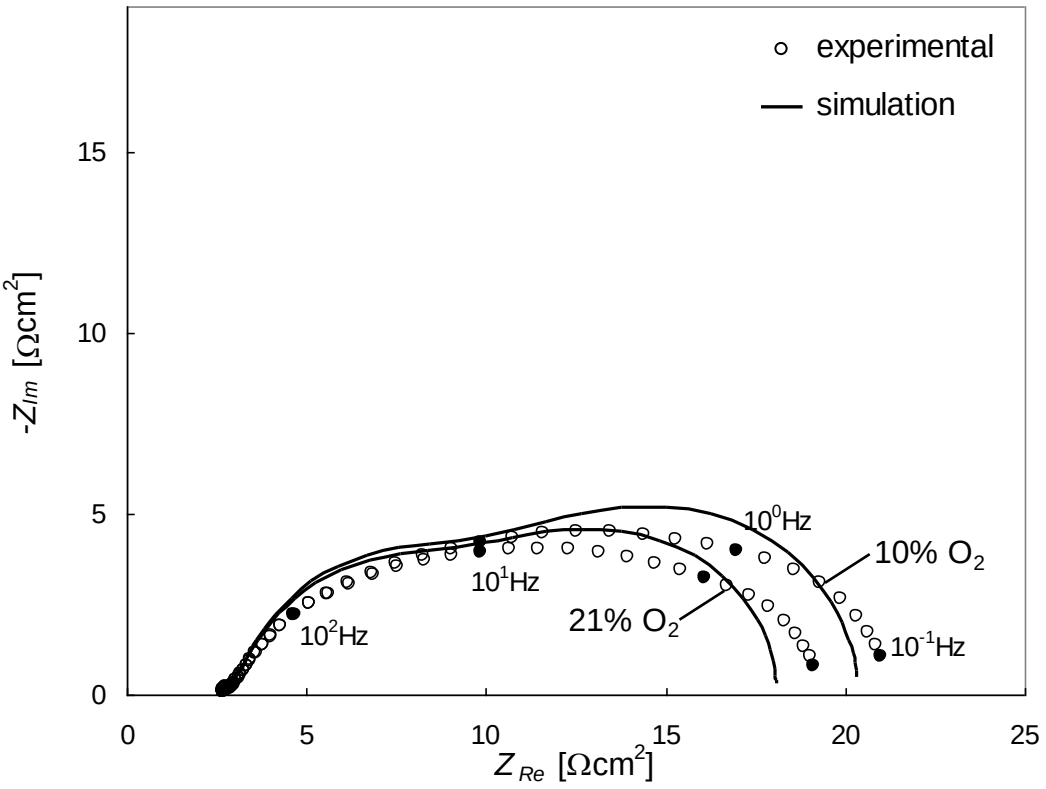

Figure 4. Calibration of the model (lines) with experimental data (circles) for different oxygen partial pressures at OCV and 750°C.

The experimental data reported in Figures 3 and 4 are used to calibrate the model by fitting the unknown parameters of the ORR. As shown with solid lines, the model

reproduces reasonably well the shape, characteristic frequency as well as temperature- and p_{O2}-dependences observed experimentally in the whole range of conditions investigated. Experimental data are not exactly reproduced by simulation results for two main reasons: i) the model represents a simplified description of reality (e.g., the microstructure is not homogeneous, the transport and reaction mechanisms may be more complex than those assumed, etc.) with the minimum number of fitting parameters, and ii) a global calibration approach is performed with a single set of parameters for all the spectra analysed, without searching for the best fit of each single spectrum. Despite these inaccuracies, the experimental trends are consistently and quantitatively reproduced by the model.

The parameters fitted in the calibration are reported in Table 2 and reproduced in Figure 5 as a function of temperature. The kinetic parameters k_{des} and i_{00} increase as temperature increases, as well as the surface diffusivity of oxygen adatoms D_s. Since kinetic and transport phenomena are expected to be thermally-activated processes, this result is reasonable. On the other hand, the equilibrium constant of oxygen adsorption K decreases as temperature increases, which is plausible because molecular oxygen is expected to be less prone to adsorb and stick on LSM as its thermal energy increases. The capacitance c_{TPB} remains almost constant with temperature and does not show a clear trend. However, since c_{TPB} is a lumped parameter taking into account all the capacitive contributions related to reaction intermediates in the charge-transfer reaction at TPB, an intuitive temperature-dependence is not necessarily expected. Finally, both the number of adsorption sites per unit of LSM surface Γ and the transfer coefficient α remain constant with temperature.

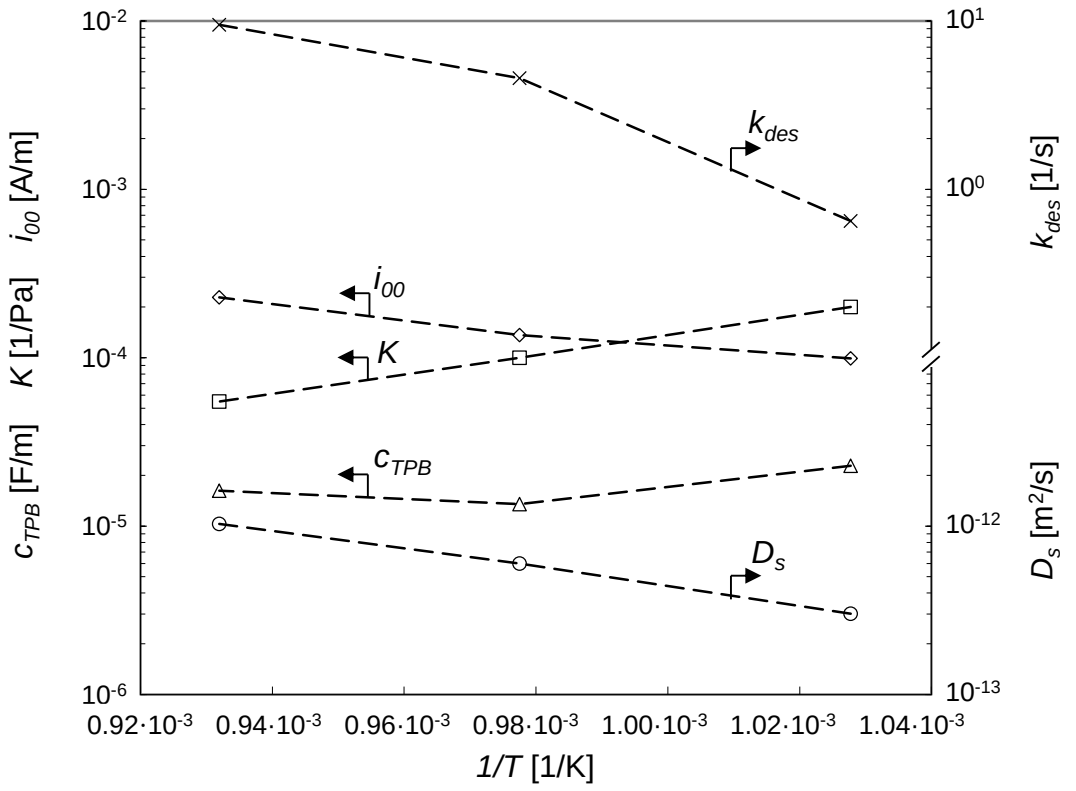

Figure 5. Arrhenius plot of the fitted parameters reported in Table 2.

Table 2. Material-specific parameters fitted on experimental spectra with the model as a function of temperature. The values of activation energy E_{act} in brackets refer to trends not properly linear in the Arrhenius plot (see Figure 5).

Parameter	**700°C**	**750°C**	**800°C**	E_{act} **[kJ/mol]**
k_{des} [1/s]	0.648	4.569	9.471	(234)
K [1/Pa]	$2.0\cdot10^{-4}$	$1.0\cdot10^{-4}$	$0.55\cdot10^{-4}$	-112
D_s [m^2/s]	$3.0\cdot10^{-13}$	$6.0\cdot10^{-13}$	$10.3\cdot10^{-13}$	106
i_{00} [A/m]	$0.99\cdot10^{-4}$	$1.36\cdot10^{-4}$	$2.28\cdot10^{-4}$	72
c_{TPB} [F/m]	$2.28\cdot10^{-5}$	$1.35\cdot10^{-5}$	$1.62\cdot10^{-5}$	(-30)
α [-]	0.75	0.75	0.75	/
Γ [mol/m^2]	$4\cdot10^{-4}$	$4\cdot10^{-4}$	$4\cdot10^{-4}$	/

The effect of the electric double layer capacitance c_{dl} on model simulations is reported in Figure 6. The figure shows the simulated Nyquist plot for two limit values: c_{dl} = 0F/m^2, i.e., no double-layer capacitance, and c_{dl} = 0.85F/m^2, as reported by Huber

et al. [8]. Note that Mitterdorfer and Gauckler [41] report an intermediate value of c_{dl} equal to 0.13 F/m^2. As shown in Figure 6, the difference between the two simulated spectra is minimal, meaning that in the operating conditions considered in this study the contribution of the electric double-layer is negligible and can be omitted. In other words, c_{dl} cannot be fitted with reasonable precision on the EIS spectra analysed above. For these reasons, in all the simulations c_{dl} is set equal to 0 since simulations results are not significantly affected by this choice.

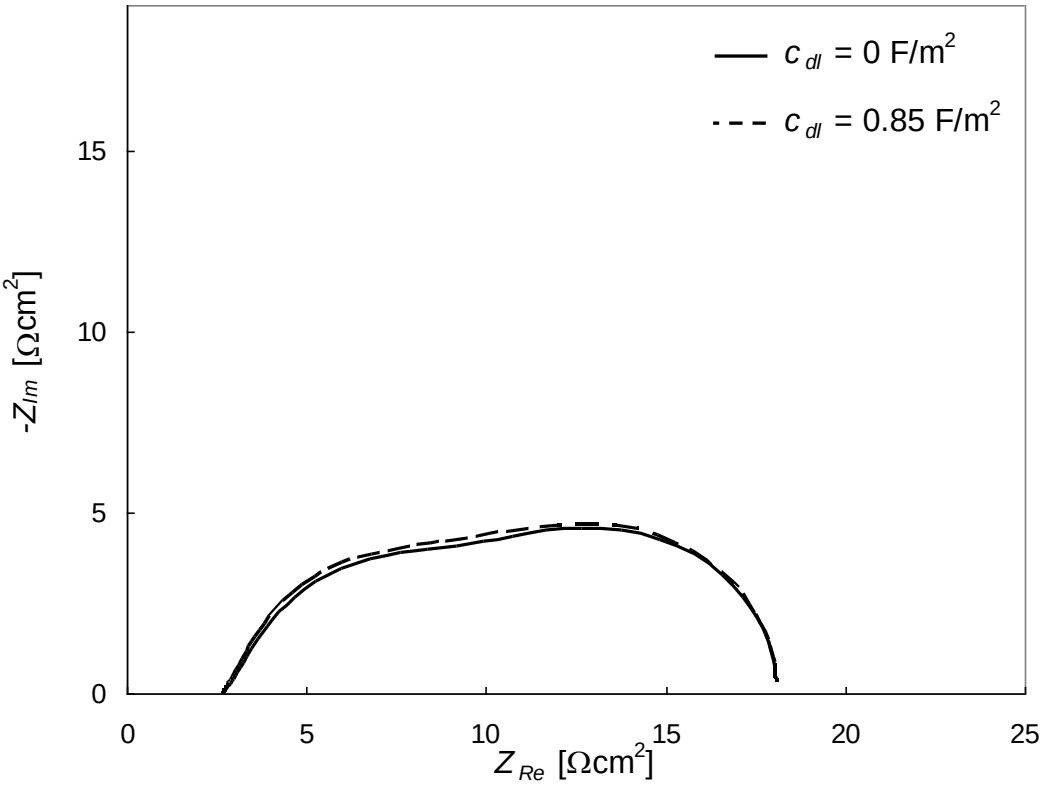

Figure 6. Effect of electric double layer capacitance c_{dl} on simulated results at OCV, 750°C and p_{O2} = 0.21atm. The simulated impedance is almost unaffected by the value of the double layer electric capacitance.

The parameters fitted during the calibration are compared with those obtained by Fu et al. [16] in composite LSM:YSZ cathodes. The specific parameters of the adsorption/diffusion process k_{des}, D_s and K are in good agreement with the values

reported by Fu et al. [16] as they fall within the same order of magnitude. In addition, the boundary layer length l_δ, which is the characteristic length representing the penetration of the adsorption/diffusion process and calculated as follows:

$$l_\delta = \sqrt{\frac{D_s}{2k_{des}\sqrt{Kp_{O2}}}} \tag{20}$$

is equal to 0.224μm at 800°C and p_{O2} = 0.21atm, which is similar to 0.29μm estimated by Fu et al. [16]. In spite of the different microstructure and fabrication process of the cathodes analysed in the two studies, the material-specific parameters of the ORR inferred from the EIS fitting are reasonably similar. It is not possible to compare i_{00} and c_{TPB} as Fu et al. [16] modelled the charge-transfer reaction at the TPB with a lumped R//C element.

Finally, it is interesting to test the predictability of the model in homogeneous composite LSM/YSZ cathodes. For the sake of conciseness, the comparison is limited to the polarization resistance calculated at OCV only. Under this equilibrium condition, the system of Eqs. (15-19) can be solved analytically to evaluate the charge-transfer resistance r_{TPB} and the resistance of the adsorption/diffusion process $r_{ads/diff}$ per unit length. By using this solution in a transmission line model [15], which considers the effective conductivity of the YSZ particles in the composite electrode σ_{io}^{eff} while neglects gas transport and the electronic resistivity of LSM, the following expressions are obtained for the polarization resistance of a composite homogeneous LSM/YSZ cathode:

$$R_p = \frac{l_\sigma}{\sigma_{io}^{eff}} \coth\left(\frac{L_c}{l_\sigma}\right) \tag{21a}$$

$$l_\sigma = \sqrt{\frac{\sigma_{io}^{eff}\left(r_{TPB} + r_{ads/diff}\right)}{\lambda_{TPB}^{v}}} \tag{21b}$$

$$r_{ads/diff} = \frac{RT}{(2F)^2}\frac{\left(1+\sqrt{Kp_{O2}}\right)^2}{\sqrt{Kp_{O2}}}\frac{l_\delta}{\Gamma D_s}\coth\left(\frac{L_s}{l_\delta}\right) \tag{21c}$$

where r_{TPB} is calculated according to Eq. (10a) (with $\bar{\theta}_0 = \theta_{eq}$) and l_δ according to Eq. (20). In Eq. (21b) λ_{TPB}^{v} represents the TPB density per unit volume while in Eq. (21c) L_s is the half-distance between two TPBs on the surface of an LSM particle in the composite cathode [16]. In particular, L_s can be estimated as $L_s = a_{el}^{v}/\lambda_{TPB}^{v}$.

The predictions of Eq. (21) are compared with the polarization resistance of composite LSM/YSZ cathodes produced and tested by Barbucci et al. [43]. The microstructural properties of the composite electrode are estimated according to the parameters and percolation model reported by Bertei et al. [45] while the material-specific parameters of the ORR are taken from Table 2. For a 45μm-thick composite LSM/YSZ cathode at OCV in air, the model predicts R_p = 0.73Ωcm^2 (700°C), 0.34Ωcm^2 (750°C) and 0.21Ωcm^2 (800°C), which are in fair agreement with the experimental values equal to 1.03Ωcm^2 (700°C), 0.58Ωcm^2 (750°C) and 0.24Ωcm^2 (800°C), respectively. The inaccuracies in the prediction of R_p are mainly attributed to the rough estimation of the microstructural properties σ_{io}^{eff}, λ_{TPB}^{v} and L_s of the composite LSM/YSZ cathode. Therefore, the predictability of the model when applied to technical electrodes can be considered satisfactory. A comprehensive discussion about the application of the model to composite LSM/YSZ cathodes is out of the scope of the paper and will be subject of further investigations.

Hence, this study confirms the goodness of the model proposed by Fu et al. [16] and provides further insights by decoupling the charge-transfer contribution with a

physically-based description and by reporting the temperature dependence of the parameters. The soundness of the parameters and their reasonable temperature dependence, the good agreement with values obtained by other manufactures with different fabrication techniques, the applicability to composite electrodes as well as the good reproduction of impedance spectra for different temperatures and oxygen partial pressures with a single set of parameters corroborate the validity of the model proposed in this study.

3.3 Transition of kinetic regime with applied dc bias

After the calibration and comparison with the literature, the model is used in this Section to predict the impedance for different applied dc overpotentials and thus to detect the transition of kinetic regime by comparison with experimental data, which is the main output of this study.

Figures 7 and 8 report the prediction of the model for different applied dc bias η_{bias} at 700 and 750°C, respectively, in comparison with experimental data. It is noteworthy that due to the ohmic resistance of the electrolyte, the dc overpotential applied to the electrode η_{bias} is smaller than the total dc overpotential applied to the cell η_{tot}, which is measured experimentally between working and reference electrode. The evaluation of η_{bias} from the measured η_{tot} is reported in the Appendix.

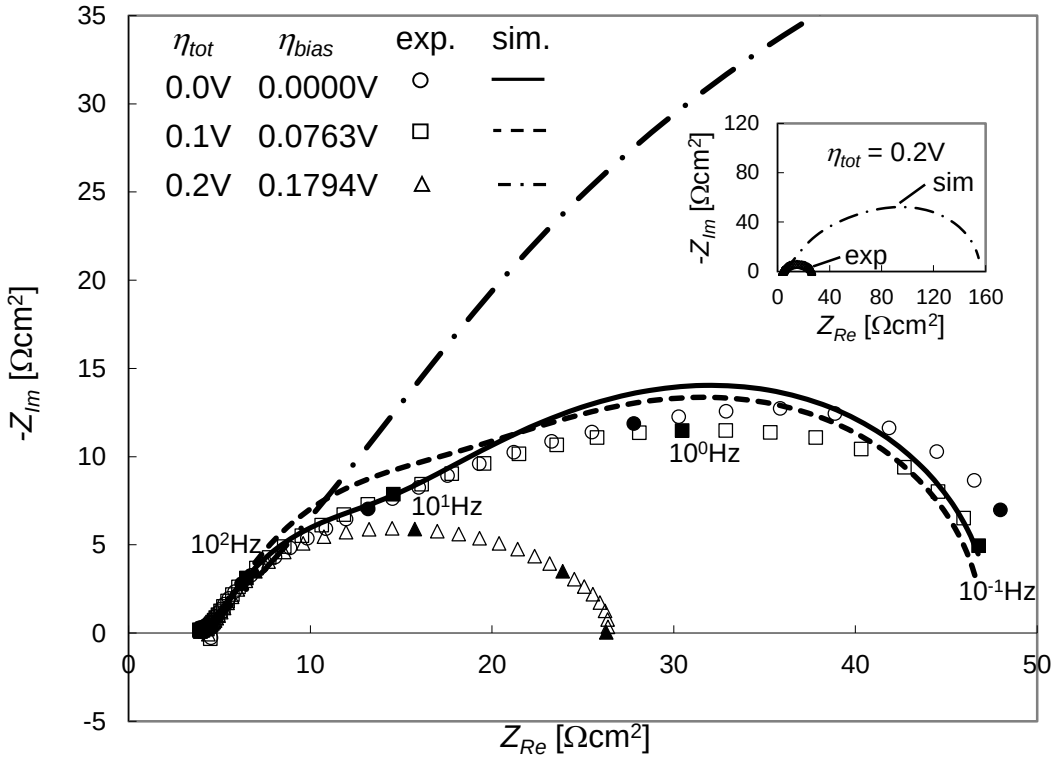

Figure 7. Impedance for different applied bias at 700°C and p_{O2} = 0.21atm as predicted by the model in comparison with experimental data.

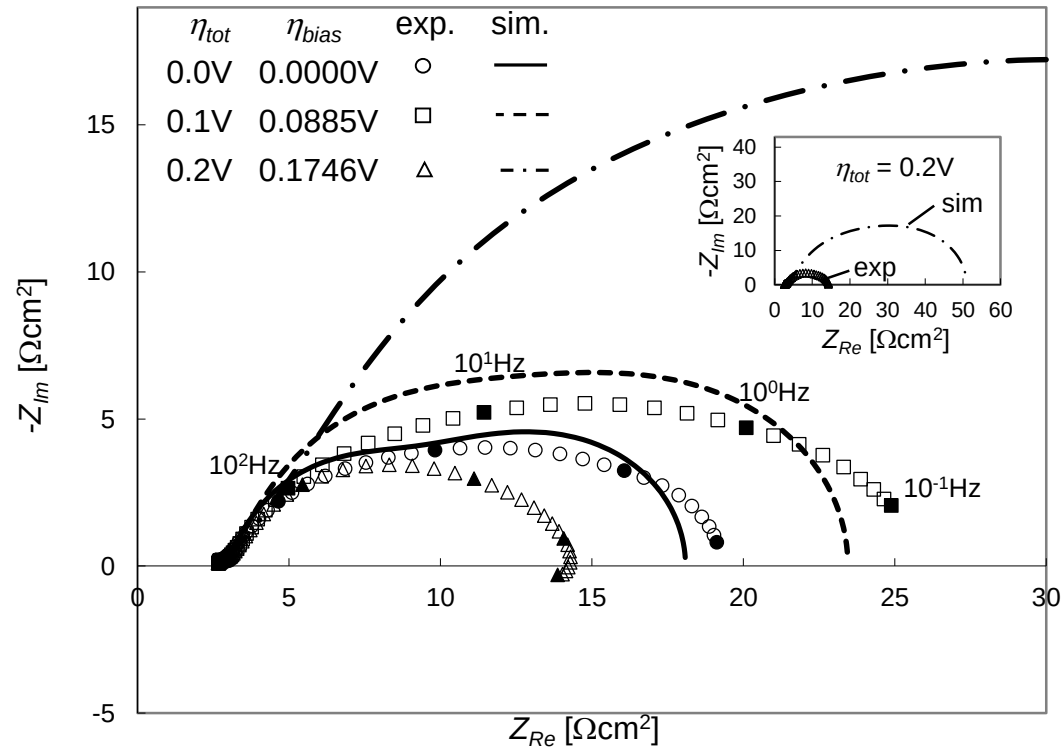

Figure 8. Impedance for different applied bias at 750°C and p_{O2} = 0.21atm as predicted by the model in comparison with experimental data.

The first interesting result concerns the change in impedance as the total dc bias increases from 0.0 to 0.1V. In the experimental data, at 700°C the polarization resistance slightly decreases as the bias increases from 0.0 to 0.1V at 700°C (Figure 7); conversely, the impedance significantly increases at 750°C (Figure 8). Without adjusting any parameters, the model reproduces these opposite behaviours fairly well at both the temperatures. In addition to the positive indications already discussed in Section 3.2, this satisfactory comparison with experimental data under current provides a further confirmation of the validity of the model.

The model can be used to provide a mechanistic explanation to the opposite trends observed in experimental data. Figure 9 shows the simulated profiles of oxygen coverage fraction for different dc overpotentials at 700 and 750°C. As the dc bias η_{bias} increases, oxygen adatoms are consumed along the cathode thickness to take part to the charge-transfer reaction at the TPB. The more oxygen adatoms are consumed, the more molecular oxygen is adsorbed according to the adsorption kinetics (see Eq. (5a)). As long as η_{bias} is small there is sufficient adsorbed oxygen to diffuse and take part to the charge-transfer reaction at the TPB, thus the increased adsorption kinetic rate leads to a global reduction in polarization resistance, as shown in the inset of Figure 9a at 700°C. However, as η_{bias} increases, oxygen is depleted from the surface of LSM (see Figure 9) and the surface diffusion becomes limiting, thus resulting in an increase in polarization resistance. The minimum of polarization resistance as a function of η_{bias} depends on θ_{eq}, which in turns depends on K (see Eq. (7)), which increases as T decreases (see Table 2 and Figure 5). Thus, the trends of R_p as function of η_{bias} for low dc overpotentials in the insets of Figure 9, associated to the counterbalance between improved adsorption and surface diffusion limitation, explain why the experimental

impedance at 700°C slightly decreases (Figure 7) while at 750°C increases (Figure 8) as the total overpotential increases from 0.0 to 0.1V.

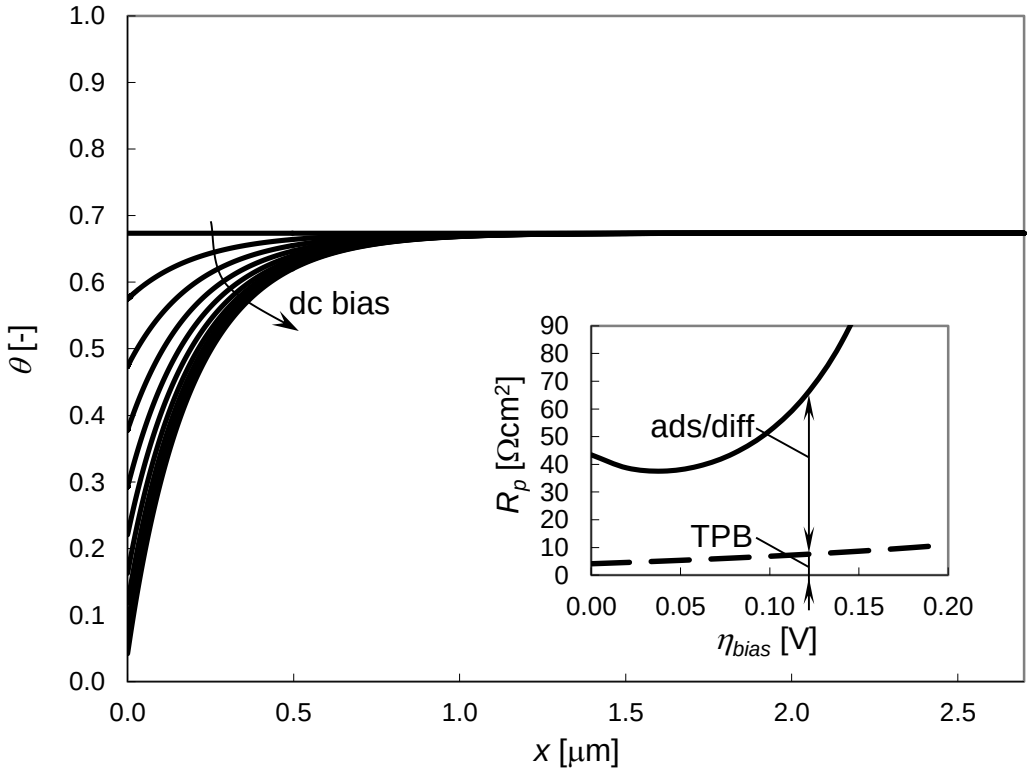

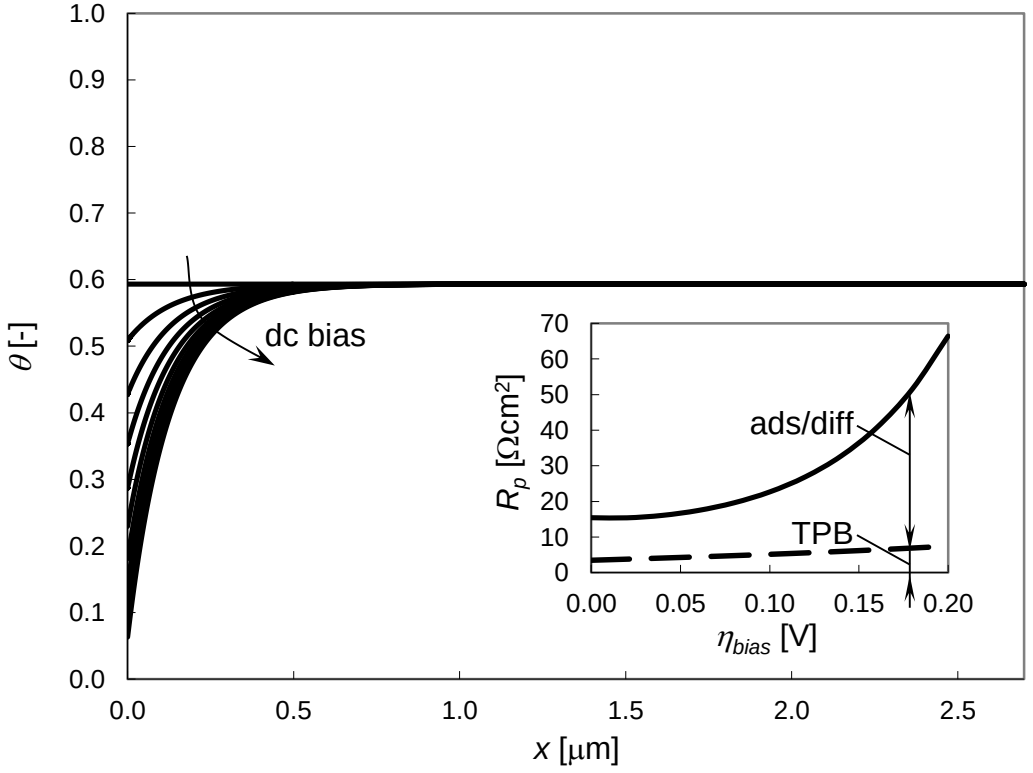

Figure 9. Simulated surface coverage of oxygen adatoms along electrode thickness for different applied dc biases η_{bias} (from 0.00V to 0.20V every 0.04V). In the inset, the electrode polarization resistance as a function of the dc bias as resulting from simulation. The operating conditions are p_{O2} = 0.21atm and a) 700°C, b) 750°C.

However, Figures 7 and 8 show that for η_{tot} = 0.2V model simulations deviate from the experimental impedance: while the simulated impedance continues to increase, the experimental data show a decrease in polarization resistance and the appearance of an inductive loop at low frequency. This disagreement is attributed to the transition from surface path to bulk path, which is not considered in the model, as explained in the following.

As already discussed in Figure 9, as the dc bias increases, oxygen is depleted from LSM surface. Eventually, considering the surface path only, a limiting current is reached as θ_0 approaches 0 at the electrode/electrolyte interface, as also proposed by Gong et al [12]. In such a case, the impedance would continue to increase, resulting in an increase in polarization resistance as shown in the inset of Figure 9. Figure 10 provides additional information based on model simulations: as η_{tot} increases, the simulated impedance increases. In particular, simulations show that the impedance is decoupled into two contributions, as already postulated in Section 3.2: a low-frequency contribution, which is due to the co-limited adsorption/diffusion process, and a medium-frequency contribution, which is related to the charge-transfer reaction at the TPB. Figure 10 shows that, as the dc bias increases, the adsorption/diffusion process becomes dominant and surface diffusion cannot supply oxygen adatoms to the TPB, resulting in a limiting current, as also reported by Gong et al. [12].

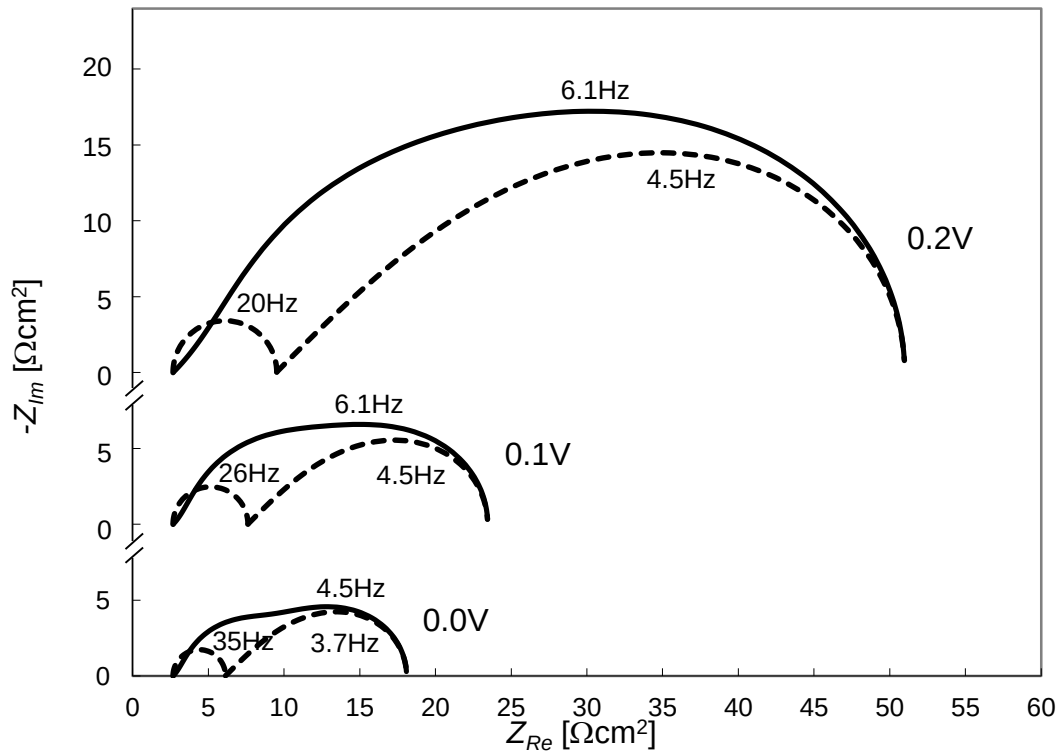

Figure 10. Decoupling of impedance with the model for different η_{tot} at 750°C and p_{O2} = 0.21atm.

However, while the model predicts a limiting current and an increase in impedance, experimental data in Figures 7 and 8 show a decrease in polarization resistance. This can be explained by considering the activation of a parallel reaction mechanism, such as the bulk path, which is able to supply oxygen ions to the electrolyte even when the surface path is in limiting conditions [12]. The transition to the bulk mechanism at η_{tot} = 0.2V is indicated not only by the decrease in impedance, but also by the presence of an inductive loop at low frequency at both 700 and 750°C in Figures 7 and 8, which has been reported by other researchers too under cathodic bias [46,47]. It is unlikely that the inductive loop be an artefact due to the misalignment of the reference electrode [48,49] because a design specifically meant to avoid such a problem was used [50], as discussed in Part 1. The activation of a parallel bulk path capable to drive the current for cathodic bias larger than 0.2V has been suggested in several studies [4,12,47,51].

More importantly, Pakalapati et al. [14] showed that, when simulating both the surface and bulk mechanisms, an inductive loop at low frequency appears in the proximity of the transition between the two regimes, in agreement with the experimental data reported in Figures 7 and 8. Despite model parameters and operating conditions simulated by Pakalapati et al. [14] may differ from those used in the experiments reported in this study, this is a further indication regarding the transition of kinetic mechanism as the dc bias increases.

Hence, the application of the model presented in Section 2 allowed for the identification of the transition of kinetic regime in the ORR in LSM, which occurs when model simulations diverge from experimental data. Considering that the model provides consistent results for different temperatures, oxygen partial pressures and low dc overpotentials (Figures 3, 4, 7 and 8), there are sound indications that the disagreement between simulations and experimental data be due to the activation of the parallel bulk path, which is also supported by the presence of an inductive low-frequency feature in experimental data.

4. Conclusions

This study presented a physically-based model of the surface path mechanism of the oxygen reduction reaction in LSM porous electrodes for the mechanistic simulation of impedance spectra.

The model was calibrated to fit the material-specific parameters of the reaction with impedance spectra measured in the range of temperature 700-800°C and oxygen partial pressure 0.10-0.21atm. The fitted material-specific parameters showed reasonable trends with temperature and agreed with previous research reported in the literature [16]. Model simulations allowed for the mechanistic deconvolution of two features in the impedance spectra: a low-frequency feature at ca. 5Hz, due to the co-limited

adsorption/diffusion of oxygen adatoms onto LSM, and a smaller medium-frequency feature at ca. 35Hz, associated to the charge-transfer reaction at the three-phase boundary with the YSZ electrolyte.

The comparison of model simulations with experimental data at different applied dc overpotentials allowed for the quantitative identification of the transition of kinetic regime, form surface to bulk path, which occurred at ca. 0.2V, in agreement with the indications reported in the literature [4,12,47,51]. In particular, the transition is highlighted by a significant decrease in polarization resistance and the appearance of a low-frequency inductive loop in experimental data. Simulations showed that, as the dc bias increases, the surface diffusion cannot supply enough adsorbed oxygen to the TPB, which would result in a limiting current if the bulk path were not activated.

The mechanistic insight provided by the model and its set of parameters estimated in this study promote a fundamental understanding of the physical-chemical phenomena of the oxygen reduction reaction. This may help the optimization of technical LSM-based composite electrodes, which normally operate at relatively low dc bias, that is, in surface path regime. In particular, since the adsorption/diffusion process is the major polarization contribution at low dc bias, a significant increase in performance is expected from the enhancement of the surface properties of LSM, as also suggested by Gong et al. [12,13] and Banerjee and Deutschmann [23]. So far the optimization of composite cathodes has mainly focused on the maximization of the TPB length [52,53]. On the other hand, this study suggests that other microstructural parameters and physical properties related to LSM surface are more important than the TPB length, such as the characteristic length of the adsorption/diffusion process, the surface diffusivity of oxygen adatoms and the adsorption constant. Optimizing these parameters may improve the performance of LSM-based electrodes beyond what

achieved so far, making them attractive also for intermediate temperature operation. The model proposed in this study can be used as a design tool to accomplish this goal.

Acknowledgements

The financial support of the Italian Minister of Education, University and Research (MIUR) National PRIN project (BIOITSOFC) is acknowledged.

Helpful discussion with Prof. Bilge Yildiz (MIT) is gratefully acknowledged.

Appendix

A.1 Calculation of dc bias from the total applied overpotential

This section summarizes the procedure used to calculate the dc overpotential η_{bias} applied to the electrode from impedance spectra, by removing the resistance contribution of the electrolyte from the total overpotential η_{tot} between working and reference electrode.

Consider a series of two resistances R_1 and R_2 as in Figure A1a. The current I circulates in the system under the total voltage V, which is split into V_1 and V_2. For any given current, the total voltage can be expressed as:

$$V = V_1 + V_2 = R_1 I + R_2 I \qquad \text{(A1)}$$

Note that R_1 and R_2 may not be constant values, for example, they may depend on the current I.

By differentiating V for I, the following relationship is obtained:

$$Z = \frac{dV}{dI} = \frac{dV_1}{dI} + \frac{dV_2}{dI} = Z_1 + Z_2 \qquad \text{(A2)}$$

where Z, Z_1 and Z_2 represent the derivatives of voltage with current. Again, note that Z, Z_1 and Z_2 may not be constant values and may depend on I.

The problem can be stated as follows: known Z, Z_1 and Z_2 for each V, the unknowns V_1, V_2 and I must be determined.

First the following definition is considered:

$$V_2(I) = \int_0^I \frac{dV_2}{dI} dI = \int_0^I Z_2 dI \qquad \text{(A3)}$$

Then, by considering from Eq. (A2) that $dI = dV / Z$, the integral in Eq. (A3) becomes as follows:

$$V_2(I) = V_2(V) = \int_0^V \frac{Z_2}{Z} dV \qquad \text{(A4)}$$

Eq. (A4) means that if the dependence of Z_2/Z as a function of V is known, for example from the analysis of impedance spectra as in Fig. A2b, where there is a clear separation between the two contributions, the voltage V_2 experienced by the (unknown) resistance R_2 can be determined for each V from Eq. (A4). Then, $V_1 = V - V_2$. Note that the relationship Z_2/Z as a function of V may be known point-wise: in such a case, the integral must be solved numerically, for example, by integrating a cubic spline linking the data points.

The procedure here described is used in this study by replacing V with η_{tot} and V_2 with η_{bias}.

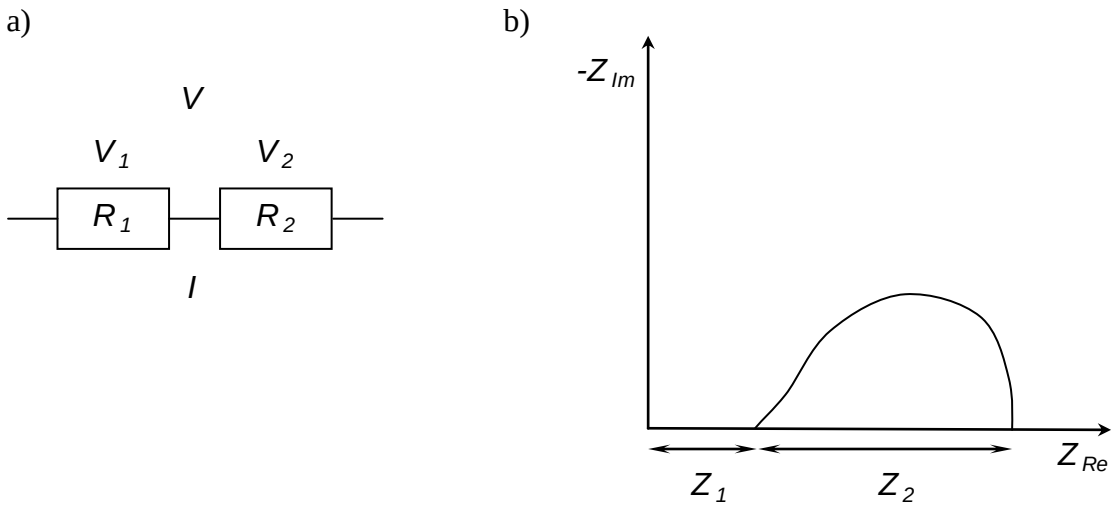

Figure A1. a) Circuit of two resistances in series. b) Example of impedance spectrum of the circuit, in which the derivatives $Z_1 = dV_1/dI$ and $Z_2 = dV_2/dI$ for each V can be unambiguously identified.

Notation

a_{el}^{v} surface area per unit volume of electron-conducting phase (1/m)

a_{dl}^{s} interfacial area between LSM and YSZ per unit of electrode area (-)

c_{dl} double-layer capacitance (F/m^2)

c_{TPB} lumped capacitance of the charge-transfer reaction at TPB (F/m)

D_s surface diffusivity of oxygen adatoms (m^2/s)

f frequency (Hz)

F Faraday constant (C/mol)

I current density (A/m^2)

i_{00} exchange current density per unit of TPB length (A/m)

i_{TPB} current density per unit of TPB length (A/m)

j imaginary unit (-)

K thermodynamic constant of oxygen adsorption/desorption equilibrium (1/Pa)

k_{des} kinetic constant of desorption reaction (1/s)

L_c cathode thickness (m)

L_s half-distance between two TPBs on the surface of an LSM particle in composite cathodes (m)

l_δ characteristic length of the adsorption/diffusion process (m)

l_σ characteristic length of the ORR/conduction process in composite cathodes (m)

N_O^{surf} molar flux of oxygen adatoms (mol/(m^{2}s))

p_{O2} oxygen partial pressure (Pa)

R gas constant (J/(mol·K))

$r_{ads/diff}$ resistance of the adsorption/diffusion process per unit length (Ωm)

R_p polarization resistance (Ωm^2)

r_{TPB} charge-transfer resistance referred per unit of TPB length (Ωm)

t time (s)

T temperature (K)

V_{el} electric potential of the electron-conducting phase (V)

V_{io} electric potential of the ion-conducting phase (V)

Z impedance (Ωm^2)

x coordinate along cathode thickness (m)

Superscripts

eff effective

Subscripts

0 electrode/electrolyte interface ($x = 0$)

el electron-conducting phase (LSM)

eq equilibrium condition

io ion-conducting phase (YSZ)

Greek letters

α transfer coefficient (-)

Γ number of adsorption sites per unit of LSM surface area (mol/m^2)

$\Delta\zeta$ ac perturbation of variable ζ

$\overline{\zeta}$ steady-state solution of variable ζ

η_{act} activation overpotential (V)

η_{bias} dc overpotential applied to the electrode (V)

η_{tot} dc overpotential applied to the electrode and electrolyte (V)

θ surface coverage fraction of oxygen adatoms (-)

λ_{TPB}^{s} TPB length per unit of electrode/electrolyte area (1/m)

λ_{TPB}^{v} TPB length per unit volume in a composite electrode (1/m^2)

σ conductivity (S/m)

τ_s surface tortuosity factor (-)

ω angular frequency (Hz)

References

[1] J. Larminie, A. Dicks, Fuel Cell Systems Explained, Wiley, New York, 2003.

[2] S.C. Singhal, K. Kendall, High temperature solid oxide fuel cells: fundamentals, design and applications, Elsevier, Oxford, 2003.

[3] S.C. Singhal, Advances in solid oxide fuel cell technology, Solid State Ionics. 135 (2000) 305–313.

[4] S.B. Adler, Factors governing oxygen reduction in solid oxide fuel cell

cathodes., Chem. Rev. 104 (2004) 4791–4843. doi:10.1021/cr020724o.

[5] C. Sun, R. Hui, J. Roller, Cathode materials for solid oxide fuel cells: A review, J. Solid State Electrochem. 14 (2010) 1125–1144. doi:10.1007/s10008-009-0932-0.

[6] J. Fleig, Solid oxide fuel cell cathodes: Polarization mechanisms and modeling of the electrochemical performance, Annu. Rev. Mater. Res. 33 (2003) 361–382. doi:10.1146/annurev.matsci.33.022802.093258.

[7] N.P. Brandon, D.J. Brett, Engineering porous materials for fuel cell applications, Philos. Trans. A. Math. Phys. Eng. Sci. 364 (2006) 147–159. doi:10.1098/rsta.2005.1684.

[8] T.M. Huber, M. Kubicek, A.K. Opitz, J. Fleig, The relevance of different oxygen reduction pathways of La0.8Sr0.2MnO3 (LSM) thin film model electrodes, J. Electrochem. Soc. 162 (2015) F229–F242. doi:10.1149/2.0061503jes.

[9] G.J. la O', B. Yildiz, S. McEuen, Y. Shao-Horn, Probing oxygen reduction reaction kinetics of Sr-doped LaMnO3 supported on Y2O3-stabilized ZrO2, J. Electrochem. Soc. 154 (2007) B427–B438. doi:10.1149/1.2508887.

[10] Y. Wu, K. V. Hansen, K. Norrman, T. Jacobsen, M. Mogensen, Oxygen electrode kinetics and surface composition of dense (La0.75Sr0.25)0.95MnO3 on YSZ, ECS Trans. 57 (2013) 1673–1682. doi:10.1149/05701.1673ecst.

[11] S.P. Jiang, A comparison of O2 reduction reactions on porous (La,Sr)MnO3 and (La,Sr)(Co,Fe)O3 electrodes, Solid State Ionics. 146 (2002) 1–22. doi:10.1016/S0167-2738(01)00997-3.

[12] M. Gong, R.S. Gemmen, X. Liu, Modeling of oxygen reduction mechanism for 3PB and 2PB pathways at solid oxide fuel cell cathode from multi-step charge transfer, J. Power Sources. 201 (2012) 204–218. doi:10.1016/j.jpowsour.2011.11.002.

[13] M. Gong, R.S. Gemmen, D.S. Mebane, K. Gerdes, X. Liu, Simulation of surface-potential driven ORR kinetics on SOFC cathode with parallel reaction pathways, J. Electrochem. Soc. 161 (2014) F344–F353. doi:10.1149/2.104403jes.

[14] S. Pakalapati, K. Gerdes, H. Finklea, M. Gong, X. Liu, I. Celik, Micro scale dynamic modeling of LSM/YSZ composite cathodes, Solid State Ionics. 258 (2014) 45–60. doi:10.1016/j.ssi.2014.01.029.

[15] J. Nielsen, J. Hjelm, Impedance of SOFC electrodes: A review and a comprehensive case study on the impedance of LSM:YSZ cathodes, Electrochim. Acta. 115 (2014) 31–45. doi:10.1016/j.electacta.2013.10.053.

[16] Y. Fu, S. Poizeau, A. Bertei, C. Qi, A. Mohanram, J.D. Pietras, et al., Heterogeneous electrocatalysis in porous cathodes of solid oxide fuel cells, Electrochim. Acta. 159 (2015) 71–80. doi:10.1016/j.electacta.2015.01.120.

[17] B. Kenney, K. Karan, Estimation of chemical and transport processes in porous, stoichiometric LSM cathodes using steady-state polarization and impedance modeling, J. Electrochem. Soc. 157 (2010) B1126–B1137. doi:Doi 10.1149/1.3432410.

[18] K. Miyoshi, T. Miyamae, H. Iwai, M. Saito, M. Kishimoto, H. Yoshida, Exchange current model for (La0.8Sr0.2)0.95MnO3 (LSM) porous cathode for

solid oxide fuel cells, J. Power Sources. 315 (2016) 63–69. doi:10.1016/j.jpowsour.2016.02.076.

[19] M.J.L. Østergård, M. Mogensen, AC impedance study of the oxygen reduction mechanism on La1-xSrxMnO3 in solid oxide fuel cells, Electrochim. Acta. 38 (1993) 2015–2020. doi:10.1016/0013-4686(93)80334-V.

[20] M.J. Jørgensen, S. Primdahl, M. Mogensen, Characterisation of composite SOFC cathodes using electrochemical impedance spectroscopy, Electrochim. Acta. 44 (1999) 4195–4201. doi:10.1016/S0013-4686(99)00134-6.

[21] V. Brichzin, J. Fleig, H.-U. Habermeier, J. Maier, Geometry dependence of cathode polarization in solid oxide fuel cells investigated by defined Sr-doped LaMnO3 microelectrodes, Electrochem. Solid-State Lett. 3 (2000) 403–406. doi:10.1149/1.1391160.

[22] A. Banerjee, O. Deutschmann, An elementary kinetic model for the electrochemical reduction of oxygen on LSM/YSZ composite cathodes, ECS Trans. 68 (2015) 713–727. doi:10.1149/06801.0713ecst.

[23] A. Banerjee, O. Deutschmann, A physical model to interpret electrochemical impedance spectra for LSM-YSZ composite cathodes, in: N.P. Brandon (Ed.), 12th Eur. SOFC Forum, Lucerne - Switzerland, 2016: pp. B0864–B0879.

[24] F.H. van Heuveln, H.J.M. Bouwmeester, F.P.F. van Berkel, Electrode properties of Sr-doped LaMnO3 on yttria-stabilized zirconia. I. Three-phase boundary area, J. Electrochem. Soc. 144 (1997) 126–133. doi:10.1149/1.1837374.

[25] F.H. van Heuveln, H.J.M. Bouwmeester, Electrode properties of Sr-doped LaMnO3 on yttria-stabilized zirconia. II. Electrode kinetics, J. Electrochem. Soc. 144 (1997) 134–140. doi:10.1149/1.1837375.

[26] M.Z. Bazant, Theory of chemical kinetics and charge transfer based on nonequilibrium thermodynamics, Acc. Chem. Res. 46 (2013) 1144–1160. doi:10.1021/ar300145c.

[27] A.J. Bard, L.R. Faulkner, Electrochemical methodes: fundamentals and applications, Wiley, New York, 2001.

[28] H. Zhu, R.J. Kee, Modeling distributed charge-transfer processes in SOFC membrane electrode assemblies, J. Electrochem. Soc. 155 (2008) B715–B729. doi:10.1149/1.2913152.

[29] W.G. Bessler, S. Gewies, M. Vogler, A new framework for physically based modeling of solid oxide fuel cells, Electrochim. Acta. 53 (2007) 1782–1800. doi:10.1016/j.electacta.2007.08.030.

[30] J. Fleig, On the current-voltage characteristics of charge transfer reactions at mixed conducting electrodes on solid electrolytes., Phys. Chem. Chem. Phys. 7 (2005) 2027–2037. doi:10.1039/B501086A.

[31] A. Bertei, J. Mertens, C. Nicolella, Electrochemical simulation of planar solid oxide fuel cells with detailed microstructural modeling, Electrochim. Acta. 146 (2014) 151–163. doi:10.1016/j.electacta.2014.08.120.

[32] J.M. Zalc, S.C. Reyes, E. Iglesia, Monte-Carlo simulations of surface and gas phase diffusion in complex porous structures, Chem. Eng. Sci. 58 (2003) 4605–4617. doi:10.1016/j.ces.2003.07.008.

[33] A. Lasia, Electrochemical impedance spectroscopy and its applications, Springer New York, New York, NY, 2014. doi:10.1007/978-1-4614-8933-7.

[34] A. Bertei, G. Arcolini, J.P. Ouweltjes, Z. Wuillemin, P. Piccardo, C. Nicolella, Physically-based deconvolution of impedance spectra: Interpretation, fitting and validation of a numerical model for lanthanum strontium cobalt ferrite-based solid oxide fuel cells, Electrochim. Acta. 208 (2016) 129–141. doi:10.1016/j.electacta.2016.04.181.

[35] J. Deseure, Y. Bultel, L. Dessemond, E. Siebert, Modelling of dc and ac responses of a planar mixed conducting oxygen electrode, Solid State Ionics. 176 (2005) 235–244. doi:10.1016/j.ssi.2004.07.018.

[36] Comsol Inc., Comsol Multiphysics user's guide, version 3.5, Burlington, MA, 2008.

[37] A. Bertei, H.W. Choi, J.G. Pharoah, C. Nicolella, Percolating behavior of sintered random packings of spheres, Powder Technol. 231 (2012) 44–53. doi:10.1016/j.powtec.2012.07.041.

[38] A. Bertei, B. Nucci, C. Nicolella, Microstructural modeling for prediction of transport properties and electrochemical performance in SOFC composite electrodes, Chem. Eng. Sci. 101 (2013) 175–190. doi:10.1016/j.ces.2013.06.032.

[39] A. Bertei, B. Nucci, C. Nicolella, Effective transport properties in random packings of spheres and agglomerates, Chem. Eng. Trans. 32 (2013) 1531–1536. doi:10.3303/CET1332256.

[40] Y. Fu, Y. Jiang, S. Poizeau, A. Dutta, A. Mohanram, J.D. Pietras, et al., Multicomponent gas diffusion in porous electrodes, J. Electrochem. Soc. 162 (2015) F613–F621. doi:10.1149/2.0911506jes.

[41] A. Mitterdorfer, L.J. Gauckler, La2Zr2O7 formation and oxygen reduction kinetics of the La0.85Sr0.15MnyO3, O2(g)|YSZ system, Solid State Ionics. 111 (1998) 185–218. doi:10.1016/S0167-2738(98)00195-7.

[42] A. Barbucci, M. Carpanese, A.P. Reverberi, G. Cerisola, M. Blanes, P.L. Cabot, et al., Influence of electrode thickness on the performance of composite electrodes for SOFC, J. Appl. Electrochem. 38 (2008) 939–945. doi:10.1007/s10800-008-9500-z.

[43] A. Barbucci, M.P. Carpanese, M. Viviani, N. Vatistas, C. Nicolella, Morphology and electrochemical activity of SOFC composite cathodes: I. Experimental analysis, J. Appl. Electrochem. 39 (2009) 513–521. doi:10.1007/s10800-008-9708-y.

[44] M.J. Jørgensen, M. Mogensen, Impedance of solid oxide fuel cell LSM/YSZ composite cathodes, J. Electrochem. Soc. 148 (2001) A433–A442. doi:10.1149/1.1360203.

[45] A. Bertei, A. Barbucci, M.P. Carpanese, M. Viviani, C. Nicolella, Morphological and electrochemical modeling of SOFC composite cathodes with distributed porosity, Chem. Eng. J. 207–208 (2012) 167–174. doi:10.1016/j.cej.2012.06.034.

[46] B. Gharbage, T. Pagnier, A. Hammou, Oxygen reduction at (La0.5Sr0.5)yMnO3 thin films/YSZ interface, Solid State Ionics. 72 (1994) 248–252. doi:10.1016/0167-2738(94)90154-6.

[47] E. Siebert, A. Hammouche, M. Kleitz, Impedance spectroscopy analysis of La1-xSrxMnO3-yttria-stabilized zirconia electrode kinetics, Electrochim. Acta. 40 (1995) 1741–1753. doi:10.1016/0013-4686(94)00361-4.

[48] S. Adler, Reference electrode placement in thin solid electrolytes, J. Electrochem. Soc. 149 (2002) E166–E172. doi:10.1149/1.1467368.

[49] J. Winkler, P.V. Hendriksen, N. Bonanos, M. Mogensen, Geometric requirements of solid electrolyte cells with a reference electrode, J. Electrochem. Soc. 145 (1998) 1184–1192. doi:10.1149/1.1838436.

[50] M. Cimenti, V.I. Birss, J.M. Hill, Distortions in electrochemical impedance spectroscopy measurements using 3-electrode methods in SOFC. II. Effect of electrode activity and relaxation times, Fuel Cells. 7 (2007) 377–391. doi:10.1002/fuce.200700020.

[51] H. Lauret, a. Hammou, Localization of oxygen cathodic reduction zone at lanthanum manganite/zirconia interface, J. Eur. Ceram. Soc. 16 (1996) 447–451. doi:10.1016/0955-2219(95)00119-0.

[52] B. Kenney, M. Valdmanis, C. Baker, J.G. Pharoah, K. Karan, Computation of TPB length, surface area and pore size from numerical reconstruction of composite solid oxide fuel cell electrodes, J. Power Sources. 189 (2009) 1051–1059. doi:10.1016/j.jpowsour.2008.12.145.

[53] V.A.C. Haanappel, J. Mertens, D. Rutenbeck, C. Tropartz, W. Herzhof, D. Sebold, et al., Optimisation of processing and microstructural parameters of LSM cathodes to improve the electrochemical performance of anode-supported SOFCs, J. Power Sources. 141 (2005) 216–226. doi:10.1016/j.jpowsour.2004.09.016.